Molybdenum Dichalcogenide Nanotube Arrays for Hydrogen-Evolution-Reaction Catalysis: Synergistic Effects of Sulfur and Selenium in a Core-Shell Tube Wall

Xuemei Zhou,[1] Jan Prikryl,[2] Milos Krbal, [2] Jan M. Macak,[2] Patrik Schmuki[1*]

[1]Department of Materials Science, Institute for Surface Science and Corrosion (LKO), University of Erlangen-Nuremberg, Martensstr. 7, 91058, Erlangen, Germany.

[2] Center of Materials and Nanotechnologies, Faculty of Chemical Technology, University of Pardubice, Nam. Cs. Legii 565, 530 02 Pardubice, Czech Republic.

E-mail: schmuki@ww.uni-erlangen.de.

Abstract:

The present work shows the growth and conversion of self-organized anodic Mo-oxide nanotube arrays to core-shell structures consisting of a conducting molybdenum sub-oxide core and a shell of Mo-Se/S – this structure is then investigated for electrochemical hydrogen evolution catalysis. To form the core-shell tubes, we first anneal MoO_3 nanotube arrays under vacuum conditions, to induce reduction to MoO_2. Subsequently these oxide tubes are thermally sulfurized and selenized resulting in dichalcogenide@sub-oxide structures. Under optimized conditions, the mixed dichalcogenide (selenized and sulfurized) tube walls on the conductive oxide core lead to a synergistic beneficial effect for the electrocatalytic H_2 generation from H_2SO_4 solution.

Keywords: anodization; nanotube; Mo-dichalcogenide; hydrogen evolution.

1. Introduction

Molybdenum dichalcogenides (MoX_2) have been investigated as promising functional materials for decades due to a number of unique intrinsic chemical and physical properties. [1-3] A key feature is the weak van der Waals forces between the layered Mo-X units that allows for easy ion intercalation and exfoliation of individual MoX sheets. As a result, MoX_2 structures can be used for wide range of layered devices such as transistors to lasers, [4] high energy density super-capacitors, [5] Li-ion batteries [6], and photocatalysts [7-8]. Moreover, recently MoX_2-functionalized electrodes have increasingly been studied for electrochemical hydrogen generation where MoX_2 structures can significantly reduce the overpotential for the hydrogen evolution reaction. [9-12]

Nevertheless, MoX_2 typically has a low intrinsic electrical conductivity, thus the catalyst is often decorated as a thin layer or nanoparticle powder mixtures [13-14] on a conductive nanostructured scaffold, hence providing short charge carrier and ion diffusion pathways.[9, 15-16]

The use of nanostructured MoX_2 geometries additionally delivers a high specific surface area with a high density of active sites. Most investigated for HER-catalysis are MoS_2 or $MoSe_2$. However, recent investigations of molybdenum sulfoselenides have reported that such mixed MoX_2 combinations can be even more active as the free energy of the reactive sites is optimized, particularly for S/Se ratios close to 1. [17-18]

Methods to prepare Mo dichalogenide nanostructures were pioneered more than 20 years ago by Tenne et al. [19] The most common synthetic approaches include chemical vapor deposition (CVD), [20] gas-phase reactions, [21] electrodeposition, [22] liquid exfoliation, [23] or wet-chemical template-assisted approaches. [24]

A very direct way to prepare functional nano-structured oxide electrodes is by self-organized anodization of a Mo-metal sheet. Using this approach, Mo-oxide nanotube arrays can be formed as 1D scaffolds and then be converted to chalcogenides. MoO_3 oxide nanotube structures commonly show a low electron conductivity and thus are less effective as an electrode than molybdenum sub-oxide (MoO_2) that provides a drastically higher electron-conductivity. [25-26]

In the present work, we form Mo-oxide nanotubular structures by self-ordering electrochemical anodization. [27] Then we anneal the as-anodized sample in vacuum to obtain

molybdenum sub-oxide nanostructures. The Mo sub-oxide samples are then thermally selenized and/or sulfurized to convert the oxide tube wall partially to the desired MoX_2 species.

We show that these tubes beneficially combine the HER catalytic properties of mixed MoX_2 compounds and the conductivity of the MoO_2 scaffold.

2. Experimental section

Self-ordered arrays of molybdenum oxide (MoO_3) nanotubes were grown on Mo foils of a 0.1 mm thickness and 99.6% purity. Before anodization, the foils were degreased by ultrasonication in acetone and ethanol successively, rinsed with deionized (DI) water, and dried in a nitrogen stream. Anodization was performed in a two-electrode system using a Pt sheet as a counter electrode. The MoO_3 nanotubes were prepared in glycerol-water electrolyte (volume ratio 9:1) containing 0.4 M NH_4F at 35 V for 1 h to achieve an approx.1 µm thick nanotubular film. After anodization the resulting layers were kept in the electrolyte for 3-5 min, then immersed into ethanol to remove the rest of electrolyte, and dried in nitrogen. To crystallize and reduce the samples, the substrates were annealed at 350 °C for 1 h in vacuum (further noted as MoO_2).

Selenization was then carried out in a tube furnace in a temperature range from 300 °C to 500 °C for 1 to 10 min. MoO_2 nanotube arrays and 0.2 g Se were placed into a quartz ampoule, evacuated to $2x10^{-4}$ Pa and sealed. Next, the ampoule was exposed to the target temperature with a rate 5 °C/min, equilibrated for 1 to 10 min and then gradually (within 10 hours) lowered to room temperature.

After selenization, the samples were annealed in H_2S gas at 200 °C, 300 °C and 500 °C for 2 min. Sulfurization was carried out in a tube furnace (Heraeus ROK/A6/30) in a H_2S (Linde Purity 2.5) volume flow of 6 L/h.

For the morphological characterization, a field emission scanning electron microscope (Hitachi FE-SEM S4800) equipped with an energy dispersive X-ray (EDX) analyzer was used. The length of the nanotubular array was directly obtained from SEM cross-sections. The composition and the chemical state of the anodic layers were characterized using X-ray photoelectron spectroscopy (XPS, PHI 5600, US). XRD patterns were collected using an

X'pert Philips PMD diffractometer with a Panalytical X'celerator detector, using graphite-monochromatized Cu Kα radiation (λ=1.54056Å).

For the electrochemical measurements, molybdenum-oxide (or dichalcogenide) tube arrays on the Mo foil were employed as anode, a graphite rod as counter electrode, and a saturated calomel electrode (SCE) as reference electrode. H_2 evolution measurements were carried out in 0.5 M H_2SO_4 aqueous solution. Impedance measurements were performed using a Zennium Zahner electrochemical workstation at applied voltages of 200 mV and -400 mV (vs. RHE) The conversion of the potential from SCE to RHE is E (RHE) = E (SCE) + 0.236 V @ 25°C, (in 0.5M H_2SO_4).

3. Results and discussion

Self-organized Mo-oxide tubular layers were grown on Mo metal by anodizing in a NH_4F/H_2O/glycerol electrolyte as described in the experimental section. Fig. 1a shows SEM top and cross-sectional images of the ordered tube array layers that consist of tubes that have an average diameter of ~80 nm and a length of ~ 1 μm.

In a set of preliminary experiments, these oxide tubes were selenized followed by sulfurization in H_2S gas in a range of temperatures (see experimental section). We observed that selenization at elevated temperatures such as 400 °C or 500 °C even for short times (several minutes) leads to a morphological deterioration of the nanotube layers. A typical example is shown in Fig. 1b, where severe cracks were formed in the layers. These defects were found to be detrimental for a stable electrode activity. On the contrary, at selenization temperatures <300 °C, conversion of the oxide tubes to $MoSe_2$ was barely detectable. Best results (no damage but partial conversion of the tube wall) were achieved by treating the samples at 300 °C for 10 min or 350°C for 10 min.

Fig. 1e shows an example for EDX data of such a sample. A clear Se L peak is present at an energy of ~1.4 keV, and a Se content of 5.13 at.% can be evaluated. XPS investigations for such samples show a Se concentration of 3.64 at%, i.e. a comparable concentration to EDX. This indicates that selenium is relatively uniform present over the entire tube length. Fig. 1c shows that the morphology of the layer after selenization remains intact; only a slight decrease of the layer thickness can be observed to ~ 0.7 μm due to a volume contraction during conversion.

These selenized tubes were then thermally sulfurized in H_2S gas. For elevated temperatures >400 °C, the tube walls were fully converted to MoS_2 and the Se entirely replaced. At a sulfurization temperature of 300 °C, slow sulfurization was achieved and selenium in the tube walls maintained. Fig. 1d shows that the tube walls become somewhat rougher after a H_2S treatment for 2 min. The tube morphology becomes further contracted but the treatment does not change the top diameter of the tubular structure significantly. For longer treatment times, along with a full conversion of oxide to MoS_2, also the tube walls become increasingly deformed.

XRD spectra for samples annealed under different conditions are shown in Fig. 2a. Samples in air mainly consist of MoO_3 while samples annealed in vacuum provide a clear MoO_2 diffraction pattern. One can observe small XRD peaks for non-stoichiometric Mo oxides (Mo_4O_{11}) for samples after vacuum annealing. After above described selenization and sulfurization treatments, clearly the characteristic XRD peaks for MoO_2 and Mo_4O_{11} are still present. Due to the low concentration of dichalcogenides, no peaks for $MoSe_2$ or MoS_2 can be detected for these conditions.

However, the successful selenization and sulfurization can be followed by XPS. Fig. 2b–e show the Mo3d, Se3d, O1s and S2p peaks for samples obtained before and after the H_2S treatment.

Fig. 2b shows the Mo3d peak for a sample after different steps. Compared with the sample annealed in air (that is composed of Mo^{6+} only), we observe a clear peak shift for reduced Mo (Mo^{5+x} and Mo^{4+x}) for the sample annealed in vacuum.

After selenization at 350 °C for 2 min, the tubes show a main contribution of Mo^{4+} with a peak position of 232.5 eV for Mo 3d3/2 and 229.5 eV for Mo 3d5/2. We also observe the presence of Mo^{4+x} (234.3 eV for Mo 3d3/2 and 231.1 eV for Mo 3d5/2) and Mo^{5+x} (235.7 eV for Mo 3d3/2 and 232.5 eV for Mo 3d5/2). The ratios of molybdenum peaks at different chemical valence states are shown in Fig. 2b. After the selenium treatment also a clear change of the O 1s peak in Fig. 2c can be observed that can be ascribed to an increase of surface oxygen and water contribution. The Se3d peaks in Fig. 2d are consistent with the formation of $MoSe_2$ (25.6%, 54.3 eV and 55.2 eV) and Mo-Se-O (74.4%, 55.3 eV and 56.2 eV).

After H_2S treatment an increase of Mo^{4+} can be observed. This can be ascribed to the formation of MoSSe from $MoSe_2$ or Mo oxide (e.g. Mo_4O_{11}). The higher states of Mo can be assigned to oxidized $MoSe_2$ or non-stoichiometric Mo oxide (as evident from XRD) – the

amount of higher oxidation states decreases after reaction in H_2S. Correspondingly, after sulfurization clearly an increase in the amount of oxygen at a higher binding energy (O1s at 532.2 eV) from 12.7% to 64.2% can be seen in Fig. 2c. This reflects the reduction of Mo-oxide. The Se 3d peak in Fig. 2d shows that after the H_2S treatment, the contribution of $MoSe_2$ to the peak decrease from 25.6 to 9.5% due to the transformation to MoSSe. Fig. 2e shows that sulfur introduced is present as S^{2-} (2p1/2 at 163.1 eV and 2p3/2 at 161.8 eV). Se (Se2p2p3/2) can be assigned to a peak at 160.8 eV [28]. After sulfurization, we obtain 2.41 at.% of S and 3.44 at.% of Se − i.e. selenium and sulfur are both successfully introduced to the molybdenum oxide nanotubular layers and in a ratio close to reported optimum of 1:1.

To explore these Mo(S,Se)@MoO_2 nanotube arrays as an electrode for hydrogen evolution reactions (HER), we measured polarization curves of anodic Mo-oxide layer, annealed in vacuum and after different H_2S and selenization treatments (Fig. 3a) in 0.5 M H_2SO_4.

The pure MoO_3 layer (samples annealed in air) or tubes fully converted to dichalcogenides show only a very low current density over the entire investigated potential range whereas samples after vacuum treatment show slightly higher current densities. Nevertheless, these samples were found to have a very limited morphological/chemical stability at potentials below 0 mV in 0.5M H_2SO_4. A significant increase in the stability and a clear onset of H_2 evolution current density is seen for samples after selenization at 300 °C or 350°C. For samples treated at 350 °C for 10 min a current density of 11 mA/cm^2 at -0.4 V (vs RHE) and a positive onset potential values of ~ -190 mV vs. RHE can be observed. After sulfurization, both selenized samples show a further increase of current density. The highest current densities are observed after the combined selenium and sulfur treatment − with 12.5 mA/cm^2 at -0.4 V (vs RHE). I.e., under this condition, there is a mild increase in current density compared with a sample with a sole selenium treatment.

The benefit of the combination is seen more clearly from the Tafel slopes (Fig. 3b) which reflect the electrochemical resistance for H_2 generation. Compared with oxide samples, a decrease of Tafel values can be observed for sample after selenium treatment (from 336 mV/dec for MoO_2 to 261 mV/dec for MoO_2-Se300 and 161 mV/dec for MoO_2-Se350). After sulfur treatment for MoO_2-Se300, we obtain a value of 177 mV/dec, however, for the best functionalized sample (MoO_2-Se350-H_2S300), a value of 157 mV/dec can be achieved. In comparison with some more complex catalysts reported in literature [24, 29-31] as well as pure Pt with a reported Tafel slope of 30 mV/dec [17, 32], the present results are still inferior

but demonstrate a successful strategy that can be further optimized towards a low cost HER platform.

Important is also that present samples were very stable in multiple cycling tests (Fig. 3c). Additional impedance measurements for samples after different production steps are shown in Fig. 3d. The results were fitted using a CPE modified Randles circuit [33-34] and the extracted charge transfer resistance values are given in the inset of Fig. 3d. The charge transfer resistance (R_{ct}) for the MoO_3 oxide sample is 1.52 MΩ. After reduction and conversion to chalcogenides the values are in the 1 KΩ range, i.e. drastically reduced. However, the plain oxide layers crack and get dissolved in the H_2SO_4 electrolyte at negative bias whereas chalcogenide samples remain stable.

In summary, we show a simple synthesis of anodic self-organized MoO_2 nanotube layers that can be further converted to a functional core-shell nanotube structures with a S/Se combination on the tube wall. The combination of the treatments provides synergistic functionality when the layers are used as a HER electrode. The conductivity is provided by the MoO_2 cores while the Se/S provides catalytic sites for HER activity. Overall, the work illustrates a synthetic pathway for chalcogenide platforms towards a use in electrochemical and photoelectrochemical applications.

Acknowledgement:

The authors would like to acknowledge ERC, DFG, Ministry of Youth, Education and Sports of the Czech Republic and the Erlangen DFG cluster of excellence for financial support.

References:

[1] Y. Yan, B. Xia, Z. Xu, X. Wang, Recent Development of Molybdenum Sulfides as Advanced Electrocatalysts for Hydrogen Evolution Reaction, ACS Catal. 4 (2014) 1693–1705.

[2] J.D. Benck, T.R. Hellstern, J. Kibsgaard, P. Chakthranont, T.F. Jaramillo, Catalyzing the Hydrogen Evolution Reaction (HER) with Molybdenum Sulfide Nanomaterials, ACS Catal. 4 (2014) 3957–3971.

[3] X. Huang, Z. Zeng, H. Zhang, Metal dichalcogenide nanosheets: preparation, properties and applications., Chem. Soc. Rev. 42 (2013) 1934–1946. doi:10.1039/c2cs35387c.

[4] R. Kappera, D. Voiry, S.E. Yalcin, B. Branch, G. Gupta, A.D. Mohite, M. Chhowalla, Phase-engineered low-resistance contacts for ultrathin MoS_2 transistors., Nat. Mater. 13 (2014) 1128–1134. doi:10.1038/nmat4080.

[5] M. Acerce, D. Voiry, M. Chhowalla, Metallic 1T phase MoS_2 nanosheets as supercapacitor electrode materials, Nat. Nanotechnol. 10 (2015) 313–318. doi:10.1038/nnano.2015.40.

[6] T. Stephenson, Z. Li, B. Olsen, D. Mitlin, Lithium ion battery applications of molybdenum disulfide (MoS_2) nanocomposites, Energy Environ. Sci. 7 (2014) 209–231. doi:10.1039/c3ee42591f.

[7] W. Zhou, Z. Yin, Y. Du, X. Huang, Z. Zeng, Z. Fan, H. Liu, J. Wang, H. Zhang, Synthesis of few-layer MoS_2 nanosheet-coated TiO_2 nanobelt heterostructures for enhanced photocatalytic activities, Small. 9 (2013) 140–147. doi:10.1002/smll.201201161.

[8] E. Parzinger, B. Miller, B. Blaschke, J.A. Garrido, J.W. Ager, A. Holleitner, U. Wurstbauer, Photocatalytic Stability of Single- and Few-Layer MoS_2, ACS Nano. 9 (2015) 11302–11309. doi:10.1021/acsnano.5b04979.

[9] H. Tang, K. Dou, C. Kaun, Q. Kuang, S. Yang, MoSe nanosheets and their graphene hybrids: synthesis, characterization and hydrogen evolution reaction studies, J. Mater. Chem. A. 2 (2014) 360–364. doi:10.1039/c3ta13584e.

[10] X. Chia, A.Y.S. Eng, A. Ambrosi, S.M. Tan, M. Pumera, Electrochemistry of Nanostructured Layered Transition-Metal Dichalcogenides, Chem. Rev. 115 (2015) 11941–11966. doi:10.1021/acs.chemrev.5b00287.

[11] F. Reale, K. Sharda, C. Mattevi, From bulk crystals to atomically thin layers of group VI-transition metal dichalcogenides vapour phase synthesis, Appl. Mater. Today. 3 (2016) 11–22. doi:10.1016/j.apmt.2015.12.003.

[12] Z. He, W. Que, Molybdenum disulfide nanomaterials: Structures, properties, synthesis and recent progress on hydrogen evolution reaction, Appl. Mater. Today. 3 (2016) 23–

56. doi:10.1016/j.apmt.2016.02.001.

[13] N. Mohamad Latiff, L. Wang, C.C. Mayorga-Martinez, Z. Sofer, A.C. Fisher, M. Pumera, Valence and oxide impurities in MoS_2 and WS_2 dramatically change their electrocatalytic activity towards proton reduction, Nanoscale. 8 (2016) 16752–16760. doi:10.1039/C6NR03086F.

[14] L. Wang, Z. Sofer, J. Luxa, M. Pumera, $Mo_xW_{1-x}S_2$ Solid Solutions as 3D Electrodes for Hydrogen Evolution Reaction, Adv. Mater. Interfaces. 2 (2015) 1500041. doi:10.1002/admi.201500041.

[15] S. Xu, Z. Lei, P. Wu, Facile preparation of 3D MoS_2 /$MoSe_2$ nanosheet–graphene networks as efficient electrocatalysts for the hydrogen evolution reaction, J. Mater. Chem. A. 3 (2015) 16337–16347. doi:10.1039/C5TA02637G.

[16] L. Jia, X. Sun, Y. Jiang, S. Yu, C. Wang, A novel $MoSe_2$-reduced graphene oxide/polyimide composite film for applications in electrocatalysis and photoelectrocatalysis hydrogen evolution, Adv. Funct. Mater. 25 (2015) 1814–1820. doi:10.1002/adfm.201401814.

[17] H. Zhou, F. Yu, Y. Huang, J. Sun, Z. Zhu, R.J. Nielsen, R. He, J. Bao, W.A. Goddard III, S. Chen, Z. Ren, Efficient hydrogen evolution by ternary molybdenum sulfoselenide particles on self-standing porous nickel diselenide foam, Nat. Commun. 7 (2016) 12765. doi:10.1038/ncomms12765.

[18] Q. Gong, L. Cheng, C. Liu, M. Zhang, Q. Feng, H. Ye, M. Zeng, L. Xie, Z. Liu, Y. Li, Ultrathin $MoS_{2(1-x)}Se_{2x}$ Alloy Nanoflakes for Electrocatalytic Hydrogen Evolution Reaction, ACS Catal. 5 (2015) 2213–2219. doi:10.1021/cs501970w.

[19] G.L. Frey, R. Tenne, Optical properties of MS_2 (M=Mo, W) inorganic fullerene-like and nanotube material optical absorption and resonance Raman measurements, J. Mater. Res. 13 (1998) 2412–2417.

[20] S. Wang, X. Wang, J.H. Warner, All Chemical Vapor Deposition Growth of MoS_2: h-BN Vertical van der Waals Heterostructures, ACS Nano. 9 (2015) 5246–5254. doi:10.1021/acsnano.5b00655.

[21] D. Kong, H. Wang, J.J. Cha, M. Pasta, K.J. Koski, J. Yao, Y. Cui, Synthesis of MoS_2 and $MoSe_2$ Films with Vertically Aligned Layers, Nano Lett. 13 (2013) 1341–1347.

doi:10.1021/nl400258t.

[22] D. Merki, S. Fierro, H. Vrubel, X. Hu, Amorphous molybdenum sulfide films as catalysts for electrochemical hydrogen production in water, Chem. Sci. 2 (2011) 1262–1267. doi:10.1039/c1sc00117e.

[23] A.Y.S. Eng, A. Ambrosi, Z. Sofer, P. Simek, M. Pumera, Electrochemistry of transition metal dichalcogenides: Strong dependence on the metal-to-chalcogen composition and exfoliation method, ACS Nano. 8 (2014) 12185–12198. doi:10.1021/nn503832j.

[24] J. Kibsgaard, T.F. Jaramillo, F. Besenbacher, Building an appropriate active-site motif into a hydrogen-evolution catalyst with thiomolybdate $[Mo_3S_{13}]^{2-}$ clusters, Nat. Chem. 6 (2014) 248–253. doi:10.1038/nchem.1853.

[25] V. Bhosle, A. Tiwari, J. Narayan, Epitaxial growth and properties of MoO_x($2<x<2.75$) films, J. Appl. Phys. 97 (2005) 083539. doi:10.1063/1.1868852.

[26] M.A.K.L. Dissanayake, L.L. Chase, Optical properties of CrO_2, MoO_2, and WO_2 in the range 0.2-6 eV, Phys. Rev. B. 18 (1978) 6872–6879. doi:10.1103/PhysRevB.18.6872.

[27] B. Jin, X. Zhou, L. Huang, M. Lickleder, M. Yang, P. Schmuki, Aligned MoO_x /MoS_2 Core-Shell Nanotubular Structures with a High Density of Reactive Sites Based on Self-Ordered Anodic Molybdenum Oxide Nanotubes, Angew.Chem.Int. Ed. 55 (2016) 12252–12256. doi:10.1002/anie.201605551.

[28] V. Kiran, D. Mukherjee, R.N. Jenjeti, S. Sampath, Active guests in the MoS_2/$MoSe_2$ host lattice: efficient hydrogen evolution using few-layer alloys of $MoS_{(2(1-x))}Se_{(2x)}$., Nanoscale. 6 (2014) 12856–12863. doi:10.1039/c4nr03716b.

[29] J. Kibsgaard, T.F. Jaramillo, Molybdenum phosphosulfide: An active, acid-stable, earth- Abundant catalyst for the hydrogen evolution reaction, Angew. Chem. Int. Ed. 53 (2014) 14433–14437. doi:10.1002/anie.201408222.

[30] M. Cabán-Acevedo, M.L. Stone, J.R. Schmidt, J.G. Thomas, Q. Ding, H.-C. Chang, M.-L. Tsai, J.-H. He, S. Jin, Efficient hydrogen evolution catalysis using ternary pyrite-type cobalt phosphosulphide., Nat. Mater. (2015) 1245–1251. doi:10.1038/nmat4410.

[31] Y. Hou, B.L. Abrams, P.C.K. Vesborg, M.E. Björketun, K. Herbst, L. Bech, A.M. Setti,

C.D. Damsgaard, T. Pedersen, O. Hansen, J. Rossmeisl, S. Dahl, J.K. Nørskov, I. Chorkendorff, Bioinspired molecular co-catalysts bonded to a silicon photocathode for solar hydrogen evolution., Nat. Mater. (2011) 434–438. doi:10.1038/nmat3008.

[32] Y. Li, H. Wang, L. Xie, Y. Liang, G. Hong, H. Dai, MoS_2 nanoparticles grown on graphene: An advanced catalyst for the hydrogen evolution reaction, J. Am. Chem. Soc. 133 (2011) 7296–7299. doi:10.1021/ja201269b.

[33] X. Zhou, V. Häublein, N. Liu, N.T. Nguyen, E.M. Zolnhofer, H. Tsuchiya, M.S. Killian, K. Meyer, L. Frey, P. Schmuki, TiO_2 Nanotubes: Nitrogen-Ion Implantation at Low Dose Provides Noble-Metal-Free Photocatalytic H_2-Evolution Activity, Angew. Chem. Int. Ed. 55 (2016) 3763–3767. doi:10.1002/anie.201511580.

[34] L. V Taveira, A.A. Sagüés, J.M. Macak, P. Schmuki, Impedance Behavior of TiO_2 Nanotubes Formed by Anodization in NaF Electrolytes, J. Electrochem. Soc. 155 (2008) C293–C302. doi:10.1149/1.2898503.

Figure captions:

Figure 1. SEM top and cross-sectional images for Mo-oxide nanotube arrays before and after selenization and sulfurization treatments: (a) anodic layer after annealing in vacuum at 300°C for 1 h, (b) after selenization at 500°C for 1 min, (c) after selenization at 350°C for 10 min, (d) after selenization at 350°C for 10 min and sulfurization at 300°C for 2 min. (e) EDX results for sample treated after selenization at 350°C for 10 min.

Figure 2. (a) XRD patterns for samples obtained at different steps. High resolution XPS peaks for (b) Mo3d, (c) O1s, (d) Se3d and (e) S2p. Compositions from deconvoluted peaks are given in at.%.

Figure 3. (a) Polarization curves for self-ordered MoO_2 nanotubular layers before and after sulfurization and selenization processes. Potential window is -400 mV to 100 mV (vs. RHE) with scan rate of 5 mV/s. (b) Tafel plots based on Fig. 3a. (c) Stability test for the best sample. (d) Impedance measurements for molybdenum oxide layers measured at +200 mV (vs. RHE) and functional molybdenum oxide layers obtained at -400 mV (vs. RHE). (Inset: fitted R_{ct} values from a Randle circuit with a constant phase element.)

Figure 1

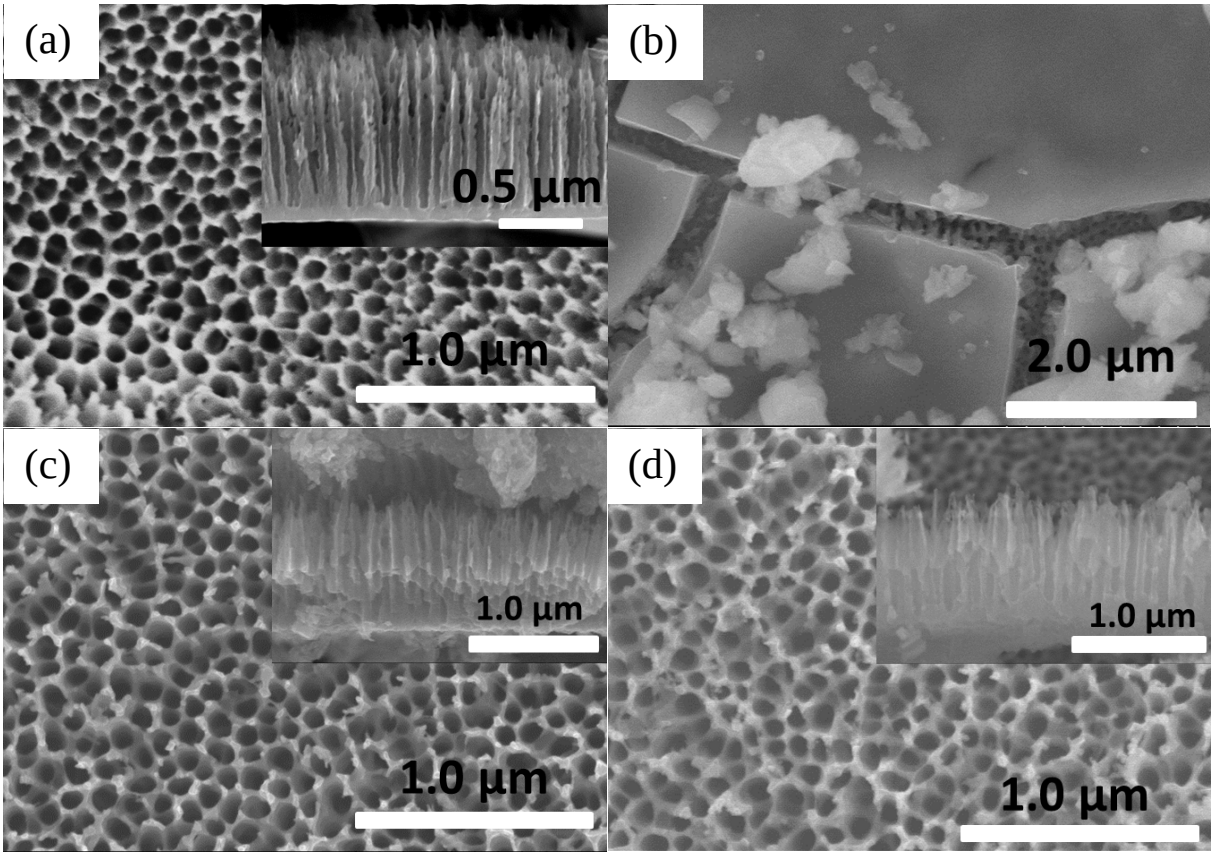
(a)
0.5 µm
1.0 µm
(b)
2.0 µm
(c)
1.0 µm
1.0 µm
(d)
1.0 µm
1.0 µm

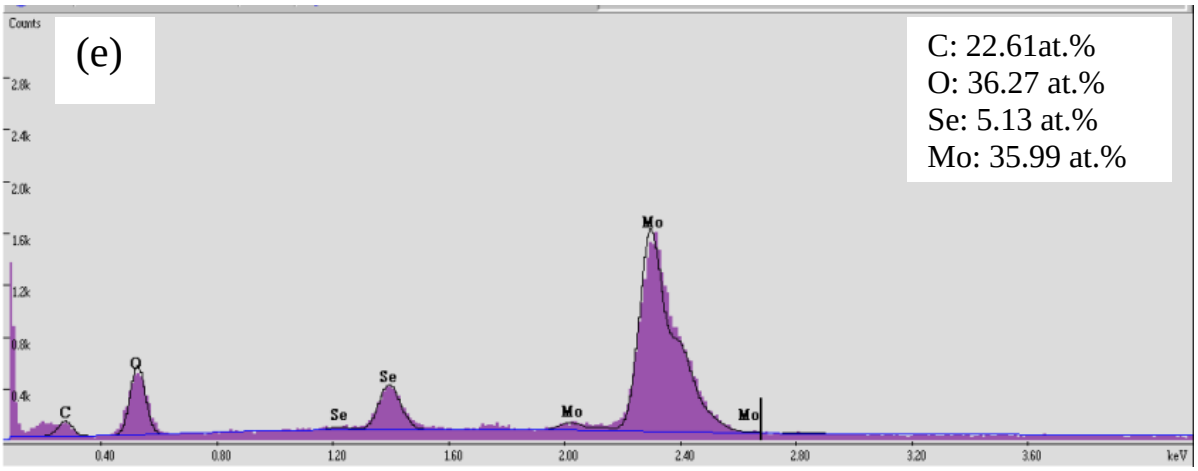
(e)
Counts
C: 22.61at.%
O: 36.27 at.%
Se: 5.13 at.%
Mo: 35.99 at.%
C
O
Se
Se
Mo
Mo
Mo
0.40
0.80
1.20
1.60
2.00
2.40
2.80
3.20
3.60
keV

Figure 2

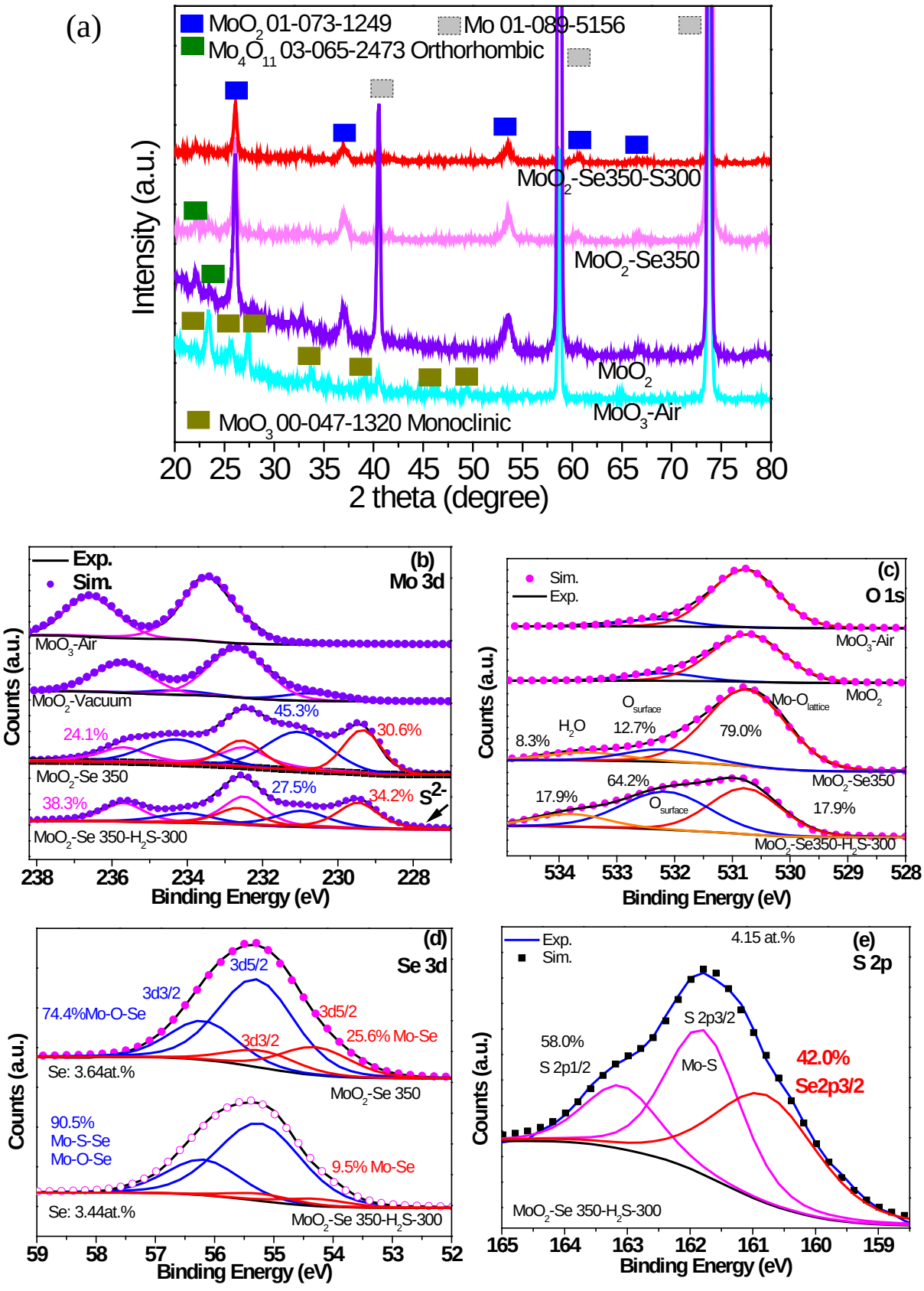
(a)
MoO2 01-073-1249
Mo 01-089-5156
Mo4O11 03-065-2473 Orthorhombic
MoO2-Se350-S300
MoO2-Se350
MoO2
MoO3-Air
MoO3 00-047-1320 Monoclinic
Intensity (a.u.)
2 theta (degree)
(b) Mo 3d
Exp.
Sim.
MoO3-Air
MoO2-Vacuum
45.3%
24.1%
30.6%
MoO2-Se 350
27.5%
38.3%
34.2%
S2-
MoO2-Se 350-H2S-300
Counts (a.u.)
Binding Energy (eV)
(c) O 1s
Sim.
Exp.
MoO3-Air
MoO2
Osurface
Mo-Olattice
H2O
12.7%
79.0%
8.3%
MoO2-Se350
64.2%
17.9%
Osurface
17.9%
MoO2-Se350-H2S-300
Counts (a.u.)
Binding Energy (eV)
(d) Se 3d
3d5/2
3d3/2
74.4%Mo-O-Se
3d5/2
3d3/2
25.6% Mo-Se
Se: 3.64at.%
MoO2-Se 350
90.5%
Mo-S-Se
Mo-O-Se
9.5% Mo-Se
Se: 3.44at.%
MoO2-Se 350-H2S-300
Counts (a.u.)
Binding Energy (eV)
(e) S 2p
Exp.
Sim.
4.15 at.%
S 2p3/2
58.0%
S 2p1/2
Mo-S
42.0%
Se2p3/2
MoO2-Se 350-H2S-300
Counts (a.u.)
Binding Energy (eV)

Figure 3

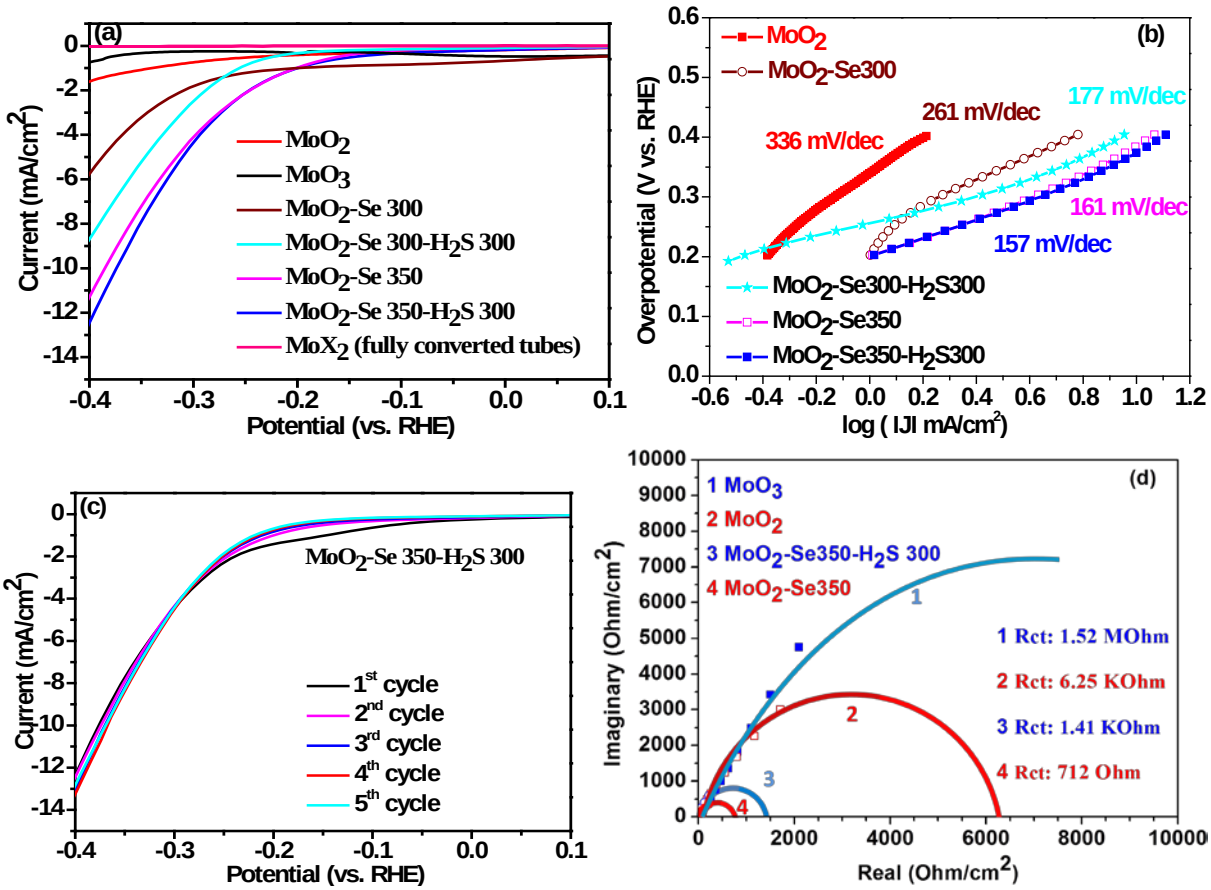
(a)
Current (mA/cm2)
Potential (vs. RHE)
MoO2
MoO3
MoO2-Se 300
MoO2-Se 300-H2S 300
MoO2-Se 350
MoO2-Se 350-H2S 300
MoX2 (fully converted tubes)
(b)
Overpotential (V vs. RHE)
log (IJI mA/cm2)
MoO2
MoO2-Se300
336 mV/dec
261 mV/dec
177 mV/dec
161 mV/dec
157 mV/dec
MoO2-Se300-H2S300
MoO2-Se350
MoO2-Se350-H2S300
(c)
Current (mA/cm2)
Potential (vs. RHE)
MoO2-Se 350-H2S 300
1st cycle
2nd cycle
3rd cycle
4th cycle
5th cycle
(d)
Imaginary (Ohm/cm2)
Real (Ohm/cm2)
1 MoO3
2 MoO2
3 MoO2-Se350-H2S 300
4 MoO2-Se350
1 Rct: 1.52 MOhm
2 Rct: 6.25 KOhm
3 Rct: 1.41 KOhm
4 Rct: 712 Ohm